PHYSICAL REVIEW A **107**, 053101 (2023)

Role of dynamic Stark shifts in strong-field excitation and subsequent ionization

Attila Tóth,[1] Sándor Borbély,[2] Yueming Zhou,[3,*] and András Csehi[4,†]

[1] *ELI-ALPS, ELI-HU Non-Profit Ltd., Dugonics tér 13, 6720 Szeged, Hungary*

[2] *Faculty of Physics, Babeş-Bolyai University, Kogălniceanu 1, Cluj-Napoca 400084, Romania*

[3] *School of Physics and Wuhan National Laboratory for Optoelectronics, Huazhong University of Science and Technology, Wuhan 430074, China*

[4] *Department of Theoretical Physics, Faculty of Science and Technology, University of Debrecen, PO Box 400, 4002 Debrecen, Hungary*

(Received 1 March 2023; revised 6 April 2023; accepted 19 April 2023; published 1 May 2023)

The energy levels of atoms and molecules exposed to intense, short, high-frequency laser pulses undergo time-dependent distortion known as dynamic Stark shift (DSS). These level shifts are induced by the coupling with nonresonant (nonessential) states and follow the temporal intensity profile of the laser pulse. Owing to the different DSSs of the individual atomic levels, transient resonance suppressions and enhancements significantly modify the multiphoton ionization pathway, leaving clear fingerprints (asymmetry, splitting, and shifting) in the energy spectrum of emitted photoelectrons. Here we investigate this phenomenon by solving the time-dependent Schrödinger equation of the valence electron of Na and Li in increasing levels of complexity: (i) developing minimal models for two-photon transition and $(2+1)$-photon ionization, (ii) applying a spectral method without continuum-continuum couplings, and (iii) propagating the electron wave packet on a large spatial grid accounting for all possible couplings. We show that appropriately detuned transform limited pulses provide a high level of control in strong-field excitation, when the atomic levels are dynamically shifted. Furthermore, we demonstrate the role of DSSs in the multipeak structure of the Autler-Townes doublet, found when several Rabi oscillations are induced during the strong-field resonant ionization.

DOI: 10.1103/PhysRevA.107.053101

I. INTRODUCTION

Selectively steering the time evolution of atomic and molecular systems with ultrashort pulsed lasers is at the heart of coherent quantum control [1,2]. In the case of strong laser pulses, the atomic and molecular energy levels undergo time-dependent distortion known as dynamic Stark shifts (DSSs), which substantially modify the underlying physics [3–5], requiring adequate control techniques [6–9]. The emergence of these level shifts is best understood considering two-photon atomic transitions within the frames of second-order perturbation theory [10–13]. If there are no intermediate states in single-photon resonance with the optical laser, which supports many cycles, these off-resonant states can be adiabatically eliminated [14] and the resulting two-level approximation is justified. In this picture, the magnitude of the induced Stark shifts and of the two-photon Rabi frequency are primarily determined by the coupling with intermediate (nonessential) states and can be further enhanced externally by increasing the laser intensity. Due to the multicycle nature of the optical pulse, these strong-field quantities of the coupled states (the DSSs and the Rabi frequency) adiabatically follow the temporal intensity profile of the pulse.

Strong-field multiphoton excitation between two bound states is usually accompanied by ionization upon absorption of further photon(s) from the same pulse. Such resonance-enhanced multiphoton ionization (REMPI) processes are sensitive to the dynamic Stark shifts of the involved resonant states and usually manifest in a structural change of the energy spectrum of emitted electrons [15–24]. The multipeak patterns observed in the photoelectron spectra were attributed to Stark-shifted bound-state multiphoton transient resonances that give rise to interference of electron amplitudes generated on the rising and falling edge of the pulse. The interference of photoelectrons emitted at different times during the same pulse was first observed using unfocused beams to avoid the spatial intensity variation effects of the laser [20]. The interference of Rydberg states provides rich information about the dynamics in strong-field ionization [24].

Selective ionization into distinct angular momentum channels is often the focus when controlling REMPI processes. Controlled suppression and enhancement of the atomic ionization yield have been shown for both phase-modulated and transform-limited pulses [25–29]. A competition between REMPI and internal conversion was demonstrated in a polyatomic molecule using shaped ultrafast laser pulses [30].

In general, when Rabi oscillations are induced between the resonantly coupled bound states, formation of the Autler-Townes (AT) doublet [31] is observed in the photoelectron spectrum. Resonance ionization following multiple Rabi oscillations leads to further structuring of the AT doublet. There has been a debate on whether the found multipeak pattern of the AT doublet is the result of dynamic interference or it is the manifestation of Rabi oscillations, and hence the pulse

---

[*] zhouymhust@hust.edu.cn

[†] csehi.andras@science.unideb.hu

area theorem [32–41]. Recently, Simonović *et al.* [41] and Tumakov *et al.* [40] concluded that the oscillatory pattern of the spectrum remains observable even for flat-top pulses, proving that it is the manifestation of Rabi dynamics. Spectral features of the AT doublet are sensitive to the system parameters, such as the Stark shifts of interest [42] or the energy-dependent bound-continuum transition dipole moments [43]. Furthermore, these features can be controlled with ultrafast laser pulses [44–46].

In a recent experiment, the direct observation of Rabi dynamics at short wavelengths was reported [47]. Applying intense coherent XUV laser pulses from a free-electron laser, two-photon ionization (TPI) of He via a resonant excited state was considered. Augmented with theoretical calculations, the authors showed that the observed asymmetry of the AT doublet is the result of interference between the resonant and nonresonant TPI pathways. Our recent theoretical results on the role of nonessential states played in the shape of the AT doublet after TPI are in line with the above experimental observations [48].

In the present paper we consider strong-field two-photon excitation and subsequent ionization of atoms to demonstrate the role of dynamic Stark shifts played in resonance ionization. Motivated by the principal aim to relate strong-field quantities (e.g., Stark shifts, two-photon Rabi frequency, and ionization rate) and the shape of the photoelectron spectrum, we follow a step-by-step didactic procedure and apply different levels of approximations: (i) We develop minimal perturbative models that include the relevant strong-field quantities (two- and three-level approximations), (ii) we solve the Schrödinger equation in the space of many field-free eigenstates (multilevel approximation) excluding continuum-continuum couplings, and (iii) we propagate the electron wave packet in the velocity gauge to account for the ponderomotive motion of the ionized electron. Whenever it is possible, analytical considerations are also applied. To exemplify our findings, the widely studied sodium [49–53] and lithium [54–57] atoms are considered.

The structure of the paper is as follows. Section II provides the description of the theoretical models. Section III gives a detailed description of the wave-packet propagation technique. Section IV discusses the numerical and analytical results obtained. A summary is given in Sec. V.

II. THEORETICAL MODELS

In this section we introduce the theoretical framework for the strong-field two-photon transition and for the $(2+1)$-photon resonance-enhanced ionization processes studied in this work. We consider atomic sodium and lithium as concrete examples initially in their ground state $|I\rangle$ ($3s$ for Na and $2s$ for Li). Applying a coherent intense laser pulse, the systems are excited by two photons to a resonant state $|R\rangle$ of the same parity (another s state). In the case of low photon energies and not too high laser intensities, the electron dynamics is expected to take place in the bound-state manifold. However, when the photon energy is large enough to resonantly excite one of the high-lying states of the atom, ionization can happen upon absorption of an additional (third) photon. Here we investigate these two processes by developing minimal two- and three-state models, respectively (Fig. 1).

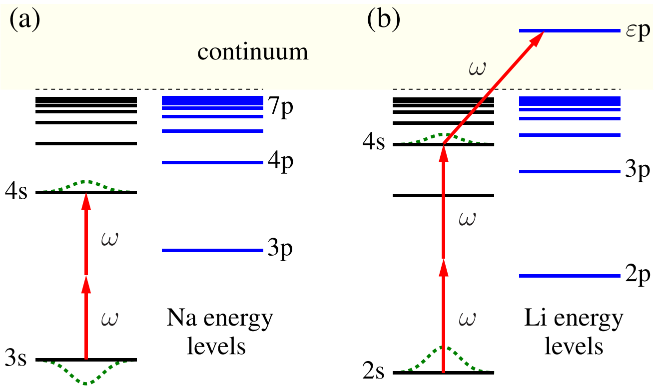

FIG. 1. Energy-level scheme of (a) sodium and (b) lithium, showing the two-photon transition and the $(2+1)$-photon resonance ionization processes discussed in this work. The bell-shaped dashed lines represent the dynamic Stark shifts of the strongly coupled atomic levels.

The field-free atom is represented by the H_0 Hamiltonian and its corresponding $|j\rangle$ eigenstates and ω_j eigenenergies ($\hbar = 1$), where the index j runs over the bound and continuum states. The interaction of the atom with the laser pulse is treated in the dipole approximation, that is, $V(t) = -\vec{\mu}\vec{\mathcal{E}}(t)$, where $\vec{\mu}$ is the transition dipole vector and $\vec{\mathcal{E}}(t)$ is the linearly polarized electric field. Throughout this work, laser pulses of the form

$$\mathcal{E}(t) = \mathcal{E}_0 g(t)\cos(\omega t) \tag{1}$$

are applied, where $\mathcal{E}_0$ is the electric-field amplitude (related to the peak intensity as $I_0 = \mathcal{E}_0^2/8\pi\alpha_{fs}$), ω is the central angular frequency, and $g(t) = e^{-t^2/2\tau^2}$ is the Gaussian envelope function (in Sec. IV, other envelope functions will be also considered). Here τ is the pulse duration that is closely related to the full width at half maximum (FWHM) equal to $2\tau\sqrt{\ln 2}$.

The total time-dependent wave function of the active electron contains both the essential and nonessential states

$$\Psi(t) = c_I(t)|I\rangle e^{-i\omega_I t} + c_R(t)|R\rangle e^{-i\omega_R t} + \sum\!\!\!\!\!\!\int_m c_m(t)|m\rangle e^{-i\omega_m t} + \int c_\varepsilon(t)|\varepsilon\rangle e^{-i\omega_\varepsilon t}\, d\omega_\varepsilon. \tag{2}$$

In Eq. (2) the initial and resonant states are denoted by $|I\rangle$ and $|R\rangle$, respectively, while the final continuum states which are populated after the ionization process, are labeled $|\varepsilon\rangle$. The nonessential $|m\rangle$ states are far from resonance and their population is negligible during the atom-field interaction. The impact of these (bound and continuum) states on the studied two-photon transition is crucial as they give rise to the dynamic Stark shifts of the resonantly coupled atomic levels (discussed below). The choice of the nonessential states is primarily determined by the parameters of the applied laser pulse.

After inserting Eq. (2) into the time-dependent Schrödinger equation (TDSE) $i\dot{\Psi} = [H_0 + V(t)]\Psi$, the following full set of coupled differential equations is obtained for the $c_j(t)$

complex amplitudes:

$$i\dot{c}_j(t) = \sum\!\!\!\!\!\!\int_k c_k(t) e^{-i\omega_{kj}t} V_{jk}(t). \tag{3}$$

Here $\omega_{kj} = \omega_k - \omega_j$ $(j, k = I, R, m, \varepsilon)$ and the light-matter interaction term is written as $V_{jk}(t) = -\mathcal{E}(t)\mu_{jk}$, with $\mu_{jk} = \langle j|\hat{z}|k\rangle$ the transition dipole moment (TDM) matrix element between the corresponding eigenstates of the atom.

The solution of Eq. (3) was carried out with the fourth-order Runge-Kutta method in a relevant subspace of the infinite electronic state manifold of the atoms. In the case of Na, the considered subspace included 67 field-free bound states with $n < 17$ and $l < 5$ principal and angular momentum quantum numbers, respectively. On the other hand, for Li, we considered 55 bound states ($n < 14$ and $l < 5$) and an additional 500 continuum states ($l < 5$) with an equidistant level spacing ($\Delta\omega_\varepsilon = 0.000\,24$ eV) for the spectrum calculations. The necessary energy levels and dipole couplings were taken from our previous works [42,53]. The time-dependent populations of the different electronic states were calculated as $p_k(t) = |c_k(t)|^2$ and a proper convergence of the numerical calculations has been ensured.

A. Two-level model of two-photon transitions

For small photon energies and moderate laser intensities, ionization and hence the last term in Eq. (2) can be safely omitted. Furthermore, invoking that the μ_{IR} and $\mu_{mm'}$ TDMs are inherently zero, Eq. (3) is greatly simplified (for the sake of simplicity the time dependence of the population amplitudes is not written out explicitly from now on):

$$i\dot{c}_I = \sum\!\!\!\!\!\!\int_m c_m e^{i\omega_{Im}t} V_{Im}(t), \tag{4a}$$

$$i\dot{c}_R = \sum\!\!\!\!\!\!\int_m c_m e^{i\omega_{Rm}t} V_{Rm}(t), \tag{4b}$$

$$i\dot{c}_m = c_I e^{-i\omega_{Im}t} V_{mI}(t) + c_R e^{-i\omega_{Rm}t} V_{mR}(t). \tag{4c}$$

As the off-resonant nonessential states rapidly oscillate during the action of the pulse, the time evolution of the c_m amplitudes can be obtained by adiabatic elimination [14]. Integrating Eq. (4c) by parts, inserting the expression found into Eqs. (4a) and (4b) and applying the two-photon rotating-wave approximation (RWA), the following two-state equation is obtained after transformation into the interaction picture (for details, see Refs. [10,53]):

$$i\begin{pmatrix} \dot{a}_I \\ \dot{a}_R \end{pmatrix} = \begin{pmatrix} 0 & \Omega_2(t)e^{i\alpha(t)} \\ \Omega_2(t)e^{-i\alpha(t)} & 0 \end{pmatrix}\begin{pmatrix} a_I \\ a_R \end{pmatrix}. \tag{5}$$

Here $\Omega_2(t)$ is the two-photon Rabi frequency (assumed real)

$$\Omega_2(t) = -\sum\!\!\!\!\!\!\int_m \frac{\mu_{Rm}\mu_{mI}}{4} \frac{\mathcal{E}_0^2 g(t)^2}{\omega_{mI} - \omega} = \Omega_2^0 g(t)^2 \tag{6}$$

and the $\alpha(t)$ atom-field phase has been introduced using the $\Delta = 2\omega - \omega_{RI}$ two-photon detuning and the $S_k(t)$ dynamic Stark shifts $(k = I, R)$

$$S_k(t) = -\sum\!\!\!\!\!\!\int_m \frac{|\mu_{km}|^2 \mathcal{E}_0^2 g(t)^2}{2} \frac{\omega_{mk}}{\omega_{mk}^2 - \omega^2} = S_k^0 g(t)^2 \tag{7}$$

making use of the definition of the relative DSS $\delta S(t) = S_R(t) - S_I(t) = \delta S_0 g(t)^2$,

$$\alpha(t) = -\int_{-\infty}^{t} \delta S(t')dt' + \Delta t. \tag{8}$$

In agreement with the findings of other works [10,12], the $\Omega_2(t)$ and $S_k(t)$ strong-field quantities follow the $\mathcal{E}_0^2 g(t)^2$ intensity envelope function of the pulse.

In view of Eq. (5), the π-pulse condition for maximal population transfer in strong laser fields implies maximizing the absolute value of the integral [7,10]

$$\kappa = \int_{-\infty}^{\infty} \Omega_2(t) e^{i\alpha(t)} dt \tag{9}$$

for a fixed area pulse

$$\Theta = \int_{-\infty}^{\infty} |\Omega_2(t)| dt = \frac{\pi}{2}. \tag{10}$$

The phase-matching technique, namely, the modulation of the field phase such that $\alpha(t)$ evolves smoothly during the atom-field interaction, was found to be an efficient way of population transfer despite the movement of atomic levels in strong laser fields [7,10]. Tailoring the phase of the field such that the variation of $\alpha(t)$ is minimal prevents Eq. (9) from vanishing and results in maximal population transfer. Here we will show that by setting Δ appropriately, compensation of the relative DSS is possible in a time-average sense, which still allows for efficient population transfer between the dynamically shifted atomic levels.

B. Three-level model of (2 + 1)-photon ionization

For large photon energies, ionization cannot be neglected and hence all the terms in Eq. (2) have to be considered. Invoking that the μ_{IR}, $\mu_{mm'}$, and $\mu_{m\varepsilon}$ TDMs are inherently zero, furthermore omitting continuum-continuum transitions as we focus on the first photopeak here, Eq. (3) is greatly simplified. Applying these considerations and also exploiting that direct ionization of the ground state is negligible for the considered photon energies (the resonant ionization pathway dominates), Eq. (3) is written as

$$i\dot{c}_I = \sum\!\!\!\!\!\!\int_m c_m e^{i\omega_{Im}t} V_{Im}(t), \tag{11a}$$

$$i\dot{c}_R = \sum\!\!\!\!\!\!\int_m c_m e^{i\omega_{Rm}t} V_{Rm}(t) + \int c_\varepsilon e^{i\omega_{R\varepsilon}t} V_{R\varepsilon}(t) d\omega_\varepsilon, \tag{11b}$$

$$i\dot{c}_m = c_I e^{-i\omega_{Im}t} V_{mI}(t) + c_R e^{-i\omega_{Rm}t} V_{mR}(t), \tag{11c}$$

$$i\dot{c}_\varepsilon = c_R e^{-i\omega_{R\varepsilon}t} V_{\varepsilon R}(t). \tag{11d}$$

Applying the RWA and the local approximation [58], the last term in Eq. (11b) can be calculated explicitly,

$$\int c_\varepsilon e^{i\omega_{R\varepsilon}t} V_{R\varepsilon}(t) d\omega_\varepsilon = -\frac{i}{2}\Gamma(t) c_R, \tag{12}$$

where $\Gamma(t) = \Gamma_0 g(t)^2$, with $\Gamma_0 = 2\pi|\mu_{R\varepsilon}\mathcal{E}_0/2|^2$ the total ionization rate of the $|R\rangle$ resonant state. The right-hand side of Eq. (11d) can be also simplified using the RWA,

$$c_R e^{-i\omega_{R\varepsilon}t} V_{\varepsilon R}(t) = c_R \Omega_1(t) e^{-i\delta t}, \tag{13}$$

where $\Omega_1(t) = -\frac{1}{2}\mu_{\varepsilon R}\mathcal{E}_0 g(t) = \Omega_1^0 g(t)$ and $\delta = \omega - \omega_{\varepsilon R}$ are the one-photon Rabi frequency and detuning, respectively. Adiabatically eliminating the nonessential states and applying the two-photon RWA, the following three-state equation is obtained:

$$i\dot{c}_I = S_I(t)c_I + \Omega_2(t)e^{i\Delta t}c_R, \tag{14a}$$

$$i\dot{c}_R = \Omega_2(t)e^{-i\Delta t}c_I + \left(S_R(t) - \frac{i}{2}\Gamma(t)\right)c_R, \tag{14b}$$

$$i\dot{c}_\varepsilon = \Omega_1(t)e^{-i\delta t}c_R. \tag{14c}$$

The Δ, $\Omega_2(t)$, and $S_k(t)$ strong-field quantities have been defined in Sec. II A.

In Eqs. (14a)–(14c), it is possible to eliminate the oscillating factors $e^{\pm i\Delta t}$ and $e^{-i\delta t}$ by redefining the amplitudes as $c_R \to c_R e^{-i\Delta t}$ and $c_\varepsilon \to c_\varepsilon e^{-i(\Delta t + \delta t)}$. Applying these changes and incorporating the $U_p(t) = \mathcal{E}_0^2 g(t)^2/4\omega^2$ ponderomotive shift of the continuum, we obtain the three-level equations

$$i\dot{c}_I = S_I(t)c_I + \Omega_2(t)c_R, \tag{15a}$$

$$i\dot{c}_R = \Omega_2(t)c_I + \left(S_R(t) - \Delta - \frac{i}{2}\Gamma(t)\right)c_R, \tag{15b}$$

$$i\dot{c}_\varepsilon = \Omega_1(t)c_R + [U_p(t) - \Delta - \delta]c_\varepsilon. \tag{15c}$$

Equations (15a)–(15c) describe the underlying physics of the $(2+1)$-photon REMPI process studied here. The energy distribution of the photoelectrons emitted after the strong-field two-photon transition upon absorption of a third photon is calculated as $w(\omega_\varepsilon) = |c_\varepsilon(t \to \infty)|^2$ after the pulse has expired. As will be discussed below, spectral features such as shifting, splitting, and asymmetry of the photopeak are strongly affected by the Stark shifts and depletion of the resonantly coupled states, which allows one to probe the bound-state dynamics.

III. TIME PROPAGATION OF THE ELECTRON WAVE PACKET

Our general framework to propagate TDSE-like multidimensional initial-value problems [53] is written in PYTHON, making use of the PETSC program package and the SLEPC library [59]. The wave functions and operators are constructed as tensor products of one-dimensional factors; thus the framework is easily extended for multidimensional problems. The TDSE of Na and Li is solved in the dipole approximation using the velocity gauge

$$i\dot{\Psi}(\vec{r},t) = \left(-\frac{\Delta}{2} + V_{\text{core}}(r) - i\vec{\mathcal{A}}(t)\cdot\vec{\nabla}\right)\Psi(\vec{r},t), \tag{16}$$

where the laser field vector potential is

$$\vec{\mathcal{A}}(t) = -\int_{-\infty}^{t}\vec{\mathcal{E}}(t')dt'. \tag{17}$$

For the single-active-electron description of Na and Li, we used the Hellmann pseudopotential [51,53,60] and the Klapisch model potential [40,42], respectively. The discretization of the problem was achieved with the time-dependent close-coupling method [61]. Considering the axial symmetry of the problem when dealing with linearly polarized pulses, the wave function is written as a partial wave expansion in terms of spherical harmonics with $m = 0$, i.e., the Legendre polynomials $[Y_l^{m=0}(\theta,\varphi) = P_l(\theta)]$, as

$$\Psi(\vec{r},t) = \sum_{l=0}^{l_{\max}} \frac{R_l(r,t)}{r}P_l(\theta). \tag{18}$$

Substituting this wave function into the time-dependent Schrödinger equation (16) and considering the polarization direction z, one obtains a set of coupled differential equations for the radial functions R_l:

$$\begin{aligned} i\frac{\partial R_l(r,t)}{\partial t} =& \left(-\frac{\partial^2}{2\partial r^2} + \frac{l(l+1)}{2r^2} + V_{\text{core}}(r)\right)R_l(r,t) - i\mathcal{A}_z(t) \\ & \times \left[\sqrt{\frac{l^2}{(2l-1)(2l+1)}}\left(\frac{\partial}{\partial r} - \frac{l}{r}\right)R_{l-1}(r,t)\right. \\ & \left. + \sqrt{\frac{(l+1)^2}{(2l+1)(2l+3)}}\left(\frac{\partial}{\partial r} + \frac{l+1}{r}\right)R_{l+1}(r,t)\right]. \end{aligned} \tag{19}$$

The radial coordinate is treated in our implementation with the finite-element discrete-variable representation (DVR) method [62] (for details, see [53]). In the present calculations the radial grid ranged from 0 to 12 000 a.u. over 12 000 equal length finite elements, with 11 DVR points on each. The size of the Legendre polynomial basis was kept with $l_{\max} = 24$. Convergence according to all numerical parameters was ensured.

The solution of Eq. (16) entails the consecutive application of the short-time propagator

$$\Psi(t + \Delta t) = U(t, t + \Delta t)\Psi(t), \tag{20}$$

where the evolution operator is

$$U(t, t + \Delta t) = e^{-iH(t)\Delta t}. \tag{21}$$

We made use of the Lanczos algorithm [63] and performed the time stepping in a Krylov subspace constructed by the repeated application of the Hamiltonian on the wave function. The Krylov space Hamiltonian is a small (typically fewer than 20 dimensions) matrix, so its diagonalization is inexpensive.

To overcome the so-called stiffness problem, we chose to employ the split-Lanczos algorithm [64]. Its strategy is to factor out the $V_c = l(l+1)/2r^2$ centrifugal potential from the Hamiltonian of Eq. (19),

$$H(t) = H_r(t) + V_c, \tag{22}$$

which is the source of the increased stiffness (for details, see [53]). The splitting of the Hamiltonian introduces an error proportional to Δt^3 due to the noncommutativity of H_r and V_c. This is, however, negligible in our calculations, where we worked with small constant time steps $\Delta t = 0.0025$ a.u. The size of our Krylov subspace was 8 throughout the whole propagation.

The population of the different nl bound electronic states was obtained upon projecting the propagated wave packet on the given eigenfunction $p_{nl}(t) = |\langle\psi_{nl}|\Psi(t)\rangle|^2$. Similarly, the photoelectron momentum distribution was obtained by projecting the wave function at the end of the pulse on the corresponding continuum waves

$$\frac{dP}{dkd\Omega_k} = |\langle\Psi_{\vec{k}}(\vec{r})|\Psi(\vec{r},t)\rangle|^2. \tag{23}$$

These continuum states are written as

$$\Psi_{\vec{k}}(\vec{r}) = \sqrt{\frac{2}{\pi}}\frac{1}{kr}\sum_{lm} i^l e^{i\sigma_l}\phi_{k,l}(r)Y_l^{m*}(\Omega_k)Y_l^m(\Omega_r), \tag{24}$$

where σ_l are the phase shifts of the different $\phi_{k,l}$ partial waves, which are the solutions of the

$$\left(-\frac{\Delta}{2}+V_{\rm core}(r)\right)\phi_{k,l}(r) = \frac{k^2}{2}\phi_{k,l}(r) \tag{25}$$

stationary Schrödinger equation. In the case of a purely Coulombic potential, i.e., the hydrogen atom, these partial waves as well as the phase shifts are analytically known. For the case of our model potentials, $\phi_{k,l}$ are obtained by numerically solving Eq. (25) with the Numerov method and normalized to the asymptotic form at $r\to\infty$ [40]. On the other hand, the phase shifts are calculated using the Wronskian theorem [65]

$$\sin(\sigma_l-\hat{\sigma}_l) = -\frac{2m}{\hbar^2 k}\int_0^\infty \hat{\phi}_{k,l}(V-\hat{V})\phi_{k,l}dr, \tag{26}$$

where $\hat{V}$, $\hat{\phi}_{k,l}$, and $\hat{\sigma}_l$ are the reference potential, radial function, and phase shift corresponding to the Coulomb case, respectively.

The ionization probability of electrons emitted with energy $\omega_\varepsilon = k^2/2$ into the unit solid angle is given by

$$\frac{dP}{d\omega_\varepsilon d\Omega_k} = \frac{1}{k}|\langle\Psi_{\vec{k}}(\vec{r})|\Psi(\vec{r},t)\rangle|^2. \tag{27}$$

The photoelectron energy spectra may be obtained by integrating the above expression over the angles or by the formula

$$\frac{dP}{d\omega_\varepsilon} = \frac{2}{\pi k^3}\sum_l\left|\int_r dr\,\phi_{k,l}^*(r)R_l(r)\right|^2. \tag{28}$$

Similarly, the angular distribution is calculated by integrating either Eq. (23) or (27) over the magnitude of the momenta or the energy, respectively.

IV. RESULTS AND DISCUSSION

In this section we present the analytical and numerical results obtained for the Na and Li atoms interacting with an intense, short, optical laser pulse [Eq. (1)]. In Sec. IV A, strong-field two-photon transitions will be considered within the bound-state manifold of the atoms. Here the two-level approximation (TLA) [Eq. (5)] and the multilevel approximation (MLA) [Eq. (3)] will be applied to demonstrate control over the population dynamics. In Sec. IV B we will study the three-photon ionization of Li involving two-photon Rabi oscillations. To reveal the effect of bound-state dynamic Stark shifts on the shape of the photoelectron spectrum, first the minimal three-level model [Eqs. (15a)–(15c)] without $U_p(t)$ will be applied and confirmed by the multilevel solution [Eq. (3)] that neglects continuum-continuum TDMs. To see the effect of the DSS of the continuum states, these multilevel spectra will be then compared to those obtained by the three-dimensional (3D) TDSE method (Sec. III), which properly accounts for the ponderomotive motion of the ionized electron making use of the velocity gauge.

A. Strong-field two-photon transitions of Na and Li

When the laser photon energy is well below the ionization potential ($\omega \ll I_p$), the ionization probability after the near-resonant two-photon transition remains negligible. This renders the TLA adequate for studying the control of two-photon excitation [10,12,13]. Let us consider the Na and Li atoms initially ($t=-\infty$) in their ground state and inspect their interaction with a single laser pulse that couples with two photons an excited state having the same parity (see Fig. 1). To be specific, we set the photon energy to resonantly excite either the $3s\to 4s$ transition of Na [$\omega = (\omega_{4s}-\omega_{3s})/2 \approx 1.589$ eV] or the $2s\to 4s$ transition of Li [$\omega = (\omega_{4s}-\omega_{2s})/2 \approx 2.169$ eV]. Owing to the dynamic Stark shifts of the coupled levels, the bare (field-free) resonance condition is strongly modified by becoming time dependent, which makes the two-photon excitation ineffective at the above frequencies. Modulating the phase of the field such that the relative DSS of the involved levels is compensated, the resonance condition can be maintained at each moment, making the two-photon transition efficient [7,10].

According to Fig. 2(a), where a complete population inversion is targeted and hence the pulse area is set to $\Theta = \pi/2$, the excited-state population after the pulse has expired is maximized when the laser is detuned appropriately. Both the TLA and MLA populations reach their maxima for $\Delta = \pm 0.76$ [solid and dotted lines in Fig. 2(a)]. The deviations between the TLA and MLA populations, which are attributed to close-lying states, e.g., the $7p$ state for Na, are minimized for longer pulses [66]. Importantly, the magnitude of the κ integral [Eq. (9)] also peaks in the same regions of the detuning parameter, indicating efficient population transfer [dashed lines in Fig. 2(a)].

The time dependence of the $\alpha(t)$ atom-field phase for a pulsed laser cannot be canceled without phase modulations [see Eq. (8)]. However, the variations in $\alpha(t)$ can be minimized even for transform limited pulses by appropriately detuning the laser photon energy from the bare resonance (see Fig. 2). For an optimal choice of the two-photon detuning ($\Delta_{\rm opt} = 0.76\times\delta S_0$) a complete population inversion is realizable, as seen in Fig. 2(a). In such a case, the relative DSS is compensated in an average sense, which still allows for efficient excitation; e.g., in the case of the $3s\to 4s$ transition of Na, for $\Delta = 0.76\times\delta S_0$ the laser is blue detuned at the beginning and at the end of the pulse, while it is red detuned in the middle. For the $2s\to 4s$ transition of Li, it is just the other way around. For an efficient population transfer, the pulse area and the accumulated atom-field phase have to be balanced between the blue- and red-detuned regions of the pulse. This makes $\Delta_{\rm opt}$ vary between 0 and δS_0, depending on the shape of the pulse envelope function.

Applying optimally detuned pulses of area $\Theta = \pi/2$, the targeted population inversion is realized when the pulse duration is sufficiently long (with the FWHM on the order of a few hundred femtoseconds). This is seen in Fig. 3, where

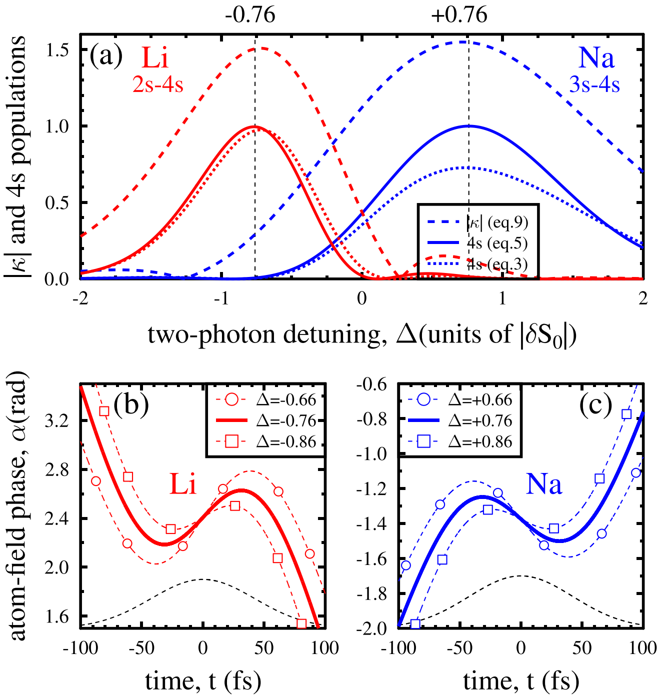

FIG. 2. (a) Final $4s$ populations of Li and Na computed in the TLA (5) (solid lines) and in the MLA (3) (dotted lines) for detuned $\pi/2$ pulses of 100-fs FWHM duration. The average relative DSS of the strongly coupled levels is compensated with negatively (Li) or positively (Na) detuned pulses that satisfy the $\Delta = 0.76\times\delta S_0$ condition (vertical dashed lines) and as a result population is efficiently transferred to the $4s$ excited levels. This is reflected by the $|\kappa|$ curves too [Eq. (9), dashed lines], which peak around the same region of the two-photon detuning. (b) Atom-field phase for Li [Eq. (8)], computed for several detuning values around the optimal one, shown in (a). (c) Same as (b) but for Na. The bell-shaped dashed lines represent the scaled intensity profile of the applied Gaussian laser pulses. The peak laser intensities were determined according to the $\pi/2$-pulse condition (10). The definition of Δ is given around Eq. (6).

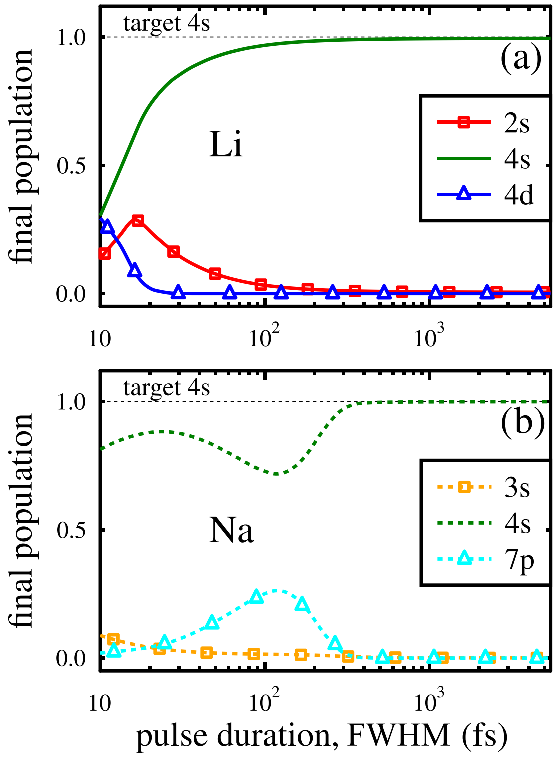

FIG. 3. Final populations of (a) Li and (b) Na computed in the multilevel approximation for detuned $\pi/2$ pulses of increasing duration. The two-photon detuning is chosen according to $\Delta_{\mathrm{opt}} = 0.76\times\delta S_0$ [see Fig. 2(a)] to induce a complete population inversion between the ground and the $4s$ levels. For short pulses, owing to the large bandwidth and the high peak intensity, several states are populated by the laser. For long enough pulses, state selectivity is fulfilled and as a result the atoms are efficiently driven to the target $4s$ state (horizontal dashed lines). The presented results were obtained by solving Eq. (3) in the space of 55 bound states for Li and 67 bound states for Na, considering the atoms initially in their ground states. For each pulse duration value, the peak laser intensity was determined according to the $\pi/2$-pulse condition (10).

the final populations of some relevant states of Na and Li are shown as a function of the pulse duration (obtained from the multilevel solution). For short pulses, owing to the large bandwidth and peak intensity, the intermediate states ($3p$ for Na and $2p$ for Li) also participate in the dynamics and as a result the desired control is not complete. In the case of Li, this leads to non-negligible population on the one-photon resonant $4d$ state, while for Na it is the $7p$ state that possesses notable population after the excitation process (for the time-dependent populations, see [66]). For longer pulses, the peak laser intensity and the pulse bandwidth are decreased and the atoms start to behave as two-level systems, making the desired control complete. The achievable final populations as well as the time-dependent populations [66] found here are similar to those obtained for phase tailored pulses [10]. This suggests that compensation for the relative DSS in an average sense can be as efficient as compensation at each moment of time when multiphoton excitations are considered. Upon increasing pulse duration, the laser bandwidth and the magnitude of the peak relative Stark shift are decreasing in synchrony, and the former always remains larger than the latter, allowing for the control by detuning. As an important manifestation of the above detuning control, we note that the bound-bound transition frequency shifts found in resonance-enhanced multiphoton ionization [51] are best approximated by Δ_{opt} rather than by δS_0. The transition frequency shift depends on the shape of the pulse envelope and is in general between 0 and δS_0 (for the presently considered Gaussian pulse shape, it is 76% of δS_0).

B. (2+1)-photon resonance ionization of Li

When the absorption of an extra photon from the same pulse leads to ionization and the pulse area is large enough to induce several Rabi oscillations, a description with the minimal three-level model [Eqs. (15a)–(15c)] is adequate [42,48]. From now on we focus exclusively on the Li atom, driven by a single laser pulse that is strong enough to induce several Rabi flops in the two-photon regime. Absorption of a third photon from the same pulse ionizes the atom and the emitted electron coherently probes the underlying dynamics. This allows us to identify the impact of the dynamic Stark shift of the involved

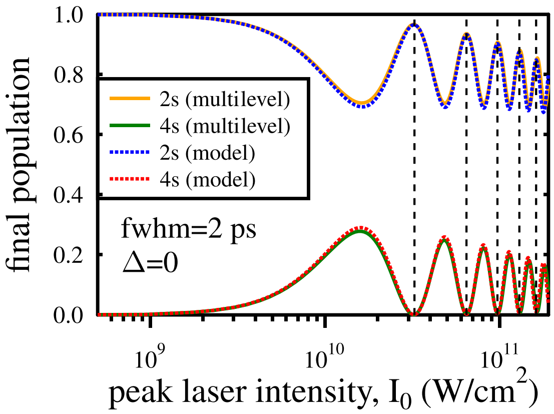

FIG. 4. Resonance-enhanced $(2+1)$-photon ionization of Li computed for two-photon resonant ($\Delta = 0 \rightarrow \omega \approx 2.169$ eV) Gaussian laser pulses of 2-ps FWHM duration. Shown are the populations of the $2s$ and $4s$ states after the pulse has expired. Upon absorption of a third photon from the same pulse, the two-photon Rabi dynamics between the resonantly coupled $2s$ and $4s$ states is damped, leading to enhanced ionization for increasing coupling strength. The vertical dashed lines indicate the laser intensities at which the system completes an integer number of Rabi cycles (for the corresponding photoelectron spectra, see Fig. 5). Note that the results obtained from the minimal three-level model [Eqs. (15a)–(15c)] are well supported by the multilevel solutions [Eq. (3)].

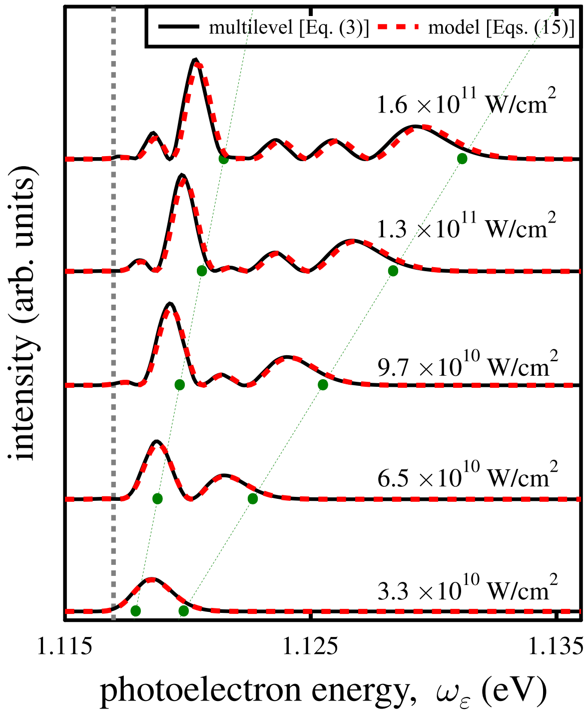

FIG. 5. Resonance-enhanced $(2+1)$-photon ionization of Li computed for two-photon resonant ($\Delta = 0 \rightarrow \omega \approx 2.169$ eV) Gaussian laser pulses of 2-ps FWHM duration. Shown are the photoelectron spectra computed for laser intensities at which the atom completes an integer number of Rabi cycles between the resonantly coupled $2s$ and $4s$ states (see the vertical dashed lines in Fig. 4). The spectral features given by the minimal three-level model [Eqs. (15a)–(15c)] are fully supported by the multilevel solutions [Eq. (3)]. The vertical dashed line indicates the nominal position of the spectra ($\omega_{\varepsilon_0} = \omega_{2s} + 3\omega$). The green circles represent the energies (at $t = 0$) given by the simple analytical model of decoupled resonances [Eq. (29)]: $\omega_{\varepsilon_0} + \mathrm{Re}[E_\pm(0)]$. For transparency, the individual spectra are vertically shifted apart from each other by factors proportional to the actual peak laser intensity.

levels on the shape of the photoelectron spectrum. For clarity, first we focus on the impact of the bound-state DSS and thus we neglect the DSS of the continuum states $U_p(t)$ in the model [36,41,43].

As we saw in the preceding section, for the minimal model description of Li to agree with the multilevel description, long pulses are required that have a narrow enough bandwidth to avoid excitation of close-lying states. Therefore, we apply the 2-ps FWHM pulse duration, and to clearly see the impact of the DSS of the $2s$ and $4s$ states, the laser is set to bare resonance $\Delta = 0$ (detuning can further control the dynamics and hence the spectral shape, to be discussed below). As shown in Fig. 4, the Li atom undergoes damped Rabi oscillations for increasing peak laser intensity. Importantly, the minimal three-level model populations are well supported by the accurate multilevel ones, which are obtained by solving Eq. (3) in the space of 55 bound and 500 unbound states, neglecting continuum-continuum TDMs to remain consistent with the model. The good agreement between the two kinds of population curves indicates that the bound-state population dynamics occurs almost exclusively between the $2s$ and $4s$ states. The very slight deviations are attributed to a minor excitation of the intermediate $2p$ state.

The photoelectron spectra computed for the peak laser intensities at which the system completes an integer number of Rabi cycles, indicated by the vertical dashed lines in Fig. 4, are shown in Fig. 5. For better visualization, these spectra are shifted apart from each other by factors proportional to the actual peak laser intensity. Clearly, when at least two Rabi cycles are completed, the spectra exhibit the AT doublet. These doublets are asymmetric and shifted to higher energies relative to the nominal peak position expected in the weak-field limit (vertical dashed line in Fig. 5): $\omega_{\varepsilon_0} = \omega_{2s} + 3\omega$. Furthermore, for increasing laser intensity the splitting of the doublets also increases and an oscillatory multipeak pattern develops in between the two prominent peaks. The number of peaks in the doublets directly reflects the number of Rabi oscillations completed by the system [41]. All these spectral features are expected to carry information on the relevant strong-field quantities involved in the preceding two-photon Rabi dynamics. Importantly, the spectra given by the minimal model are fully supported by the multilevel solutions, seen in Fig. 5. Therefore, the minimal model is suitable for identifying the impact of bound-state DSSs in the spectral shape.

A very transparent illustration of the emergence of the spectrum following resonance ionization can be given using the picture of decoupled resonances [36,41,42]. In this picture, two decaying dressed states are formed during the action of the resonant laser, the energies of which can be calculated by diagonalizing the 2×2 matrix that describes the resonant excitation on the right-hand side of Eqs. (15a) and (15b),

$$E_\pm(t) = \frac{\Sigma(t)-\Delta}{2} - \frac{i}{4}\Gamma(t) \pm \sqrt{\Omega_2^2(t) + \left(\frac{\delta S(t) - \Delta - \frac{i}{2}\Gamma(t)}{2}\right)^2}. \tag{29}$$

These quasienergies of the two decoupled resonances adiabatically follow the envelope function of the laser pulse and can be utilized to elucidate the main spectral features. In Eq. (29), the $\Sigma(t) = S_I(t) + S_R(t)$ sum of the individual Stark shifts is positive for Li ($I = 2s$ and $R = 4s$; see [66]); therefore, the spectrum is expected to be shifted towards larger energies relative to the nominal position ω_{ε_0} (note that the laser is at bare resonance $\Delta = 0$). Furthermore, the splitting of the spectrum is primarily determined by the square root in Eq. (29) when the pulse is maximal and hence the energy separation of the dressed states is the largest ($t = 0$): $\mathrm{Re}[E_+(0) - E_-(0)]$. Both the shifting and splitting of the spectrum scales linearly with the peak laser intensity, which is supported by the multilevel and model spectra as well as by the simple analytical model of decoupled resonances [Eq. (29)] seen in Fig. 5. Here the green circles indicate the peak values of the dressed-state energies relative to the nominal spectrum position: $\omega_{\varepsilon_0} + \mathrm{Re}[E_\pm(0)]$. These energy values slightly overestimate the accurate position of the spectrum since they do not take into account that electrons are emitted before and after the pulse maximum too, which contribute to lower kinetic energies. We note here that in the limit of vanishing Stark shifts the spectrum is symmetrically centered around the nominal position [36]. Here the Stark shifts are dominant, $\Gamma(t) \ll |\Omega_2(t)| \approx \frac{1}{3}\times|\delta S(t)| \approx \frac{1}{7}\times\Sigma(t)$, and leave clear fingerprints in the spectrum. They not only modify the shifting and splitting of the doublet, but strongly affect its symmetry. As will be clear below, besides the magnitude of DSSs, their temporal profile can also alter the symmetry of the AT doublet.

So far we have seen how the DSSs of the bound levels modify the spectral shape when the field is set to bare resonance. As suggested by Eq. (29), frequency modulation or detuning also affects the shape of the spectrum. Tailoring the phase of the field such that $\Sigma(t)$ is compensated, the doublet is expected to be centered around ω_{ε_0}; on the other hand, the compensation of $\delta S(t)$ is expected to cause a minimal splitting.

To see the impact of the temporal profile of the dynamic Stark shifts on the spectrum shape, we consider the general trapezoidal pulse envelope function with smooth edges [40]

$$g(t) = \begin{cases} \sin^2\left(\frac{\pi t}{2\Delta T}\right) & \text{if } 0 \leqslant t < \Delta T \\ 1 & \text{if } \Delta T \leqslant t \leqslant T - \Delta T \\ \sin^2\left(\frac{\pi(t-T)}{2\Delta T}\right) & \text{if } T - \Delta T < t \leqslant T \\ 0 & \text{if } t < 0 \text{ or } t > T, \end{cases} \tag{30}$$

where T is the total pulse duration and ΔT is the switching duration. Varying ΔT from 0 to $0.5T$, the pulse envelope in Eq. (30) is smoothly transformed from a rectangular shape to a sine-squared function, which allows us to reveal pulse shape effects. In particular, we focus on the asymmetry of the spectrum defined as $A = \frac{Q_L - Q_R}{Q_>}$, where Q_L and Q_R are the heights of the prominent leftmost and rightmost peaks of the doublet, respectively, and $Q_>$ is the larger of the two. As seen in Fig. 6(a), the asymmetry of the spectrum is strongly affected by the shape of the pulse envelope and hence the temporal profile of the DSSs. Here the pulse area is kept constant ($\Theta = 5.545\times\pi/2$) for each value of ΔT to remain consistent with the uppermost spectrum in Fig. 5 obtained for a Gaussian pulse. Similarly to the case of Gaussian pulses, the asymmetry found for a sine-squared envelope is also positive. However, for decreasing ΔT, when the intensity variations of the pulse are minimized, the asymmetry of the doublet is qualitatively modified. For flat-top pulses, when the dynamic nature of the Stark shifts is minimal, A becomes negative. Such a pulse shape dependence is never observed when the DSSs are negligible [green dashed line in Fig. 6(a)]. All these

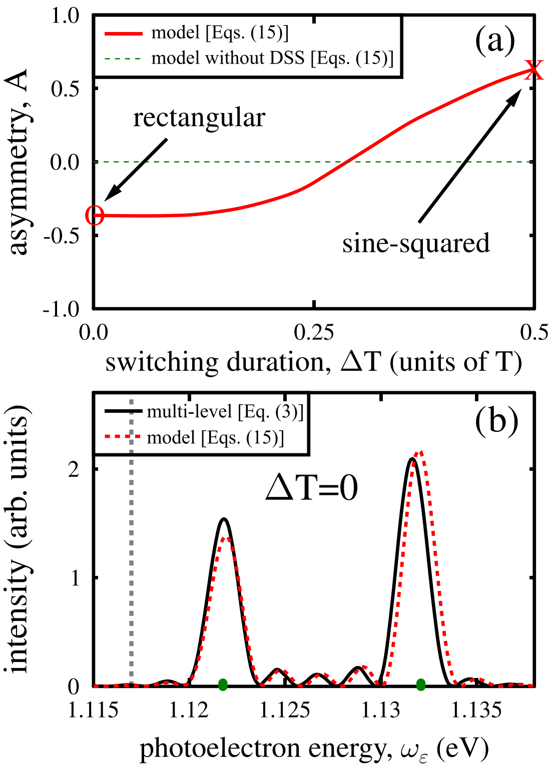

FIG. 6. (a) Asymmetry of the photoelectron spectra of Li, computed for different trapezoidal envelope functions defined in Eq. (30). When the DSSs of the resonantly coupled states are negligible, the spectrum is symmetric irrespective of the shape of the envelope (green dashed line). In contrast, when the DSSs are significant, the spectrum exhibits strong asymmetry which is very sensitive to the shape of the envelope (red solid line). (b) Photoelectron spectra computed for a rectangular pulse ($\Delta T = 0$, open circle in (a)). The observed asymmetry is opposite that found for the sine-squared [$\Delta T = 0.5$, X symbol in (a)] or Gaussian envelope shapes (Fig. 5). The slight deviations between the model and multilevel spectra are attributed to the $2p$ state. The vertical dashed line indicates the nominal position of the spectra ($\omega_{\varepsilon_0} = \omega_{2s} + 3\omega$). The laser parameters are $T = 2$ ps and $\omega \approx 2.169$ eV ($\Delta = 0$). The green circles indicate the analytical energies [Eq. (29)] $\omega_{\varepsilon_0} + \mathrm{Re}[E_\pm(0)]$. For each envelope shape, I_0 is chosen to keep the pulse area constant so as to remain consistent with the uppermost spectrum in Fig. 5 ($\Theta = 5.545\times\pi/2$).

observations suggest that besides the magnitude, the time evolution of the Stark shifts also modifies the interference of the emitted electrons and consequently affects the spectrum symmetry. Importantly, the multipeak pattern of the doublet, i.e., the manifestation of Rabi dynamics [41], remains observable in the case of a rectangular pulse, seen in Fig. 6(b). Here the qualitative change in the spectrum asymmetry predicted by the minimal model ($A < 0$) is well supported by the multilevel description. The minor deviations between the two different approaches are due to the intermediate $2p$ state in the multilevel description. As the intensity of the rectangular pulse is constant, the model of Eq. (29) can now predict the spectrum position more accurately [green circles in Fig. 6(b)] than in the case of Gaussian pulses (green circles in Fig. 5).

So far we have studied the impact of the dynamic Stark shifts of bound states on the spectral characteristics by applying the minimal model, the multilevel description, and a simple analytical model. To see the impact of the DSS of the continuum states, the ponderomotive motion of the electron has to be accounted for properly, which is conveniently done using the velocity gauge [67]. We thus solve the Schrödinger equation accurately by propagating the three-dimensional electron wave packet on a grid making use of the velocity gauge in the TDSE method (Sec. III). Comparing these TDSE spectra to those obtained by the multilevel method that neglects continuum-continuum TDMs, the effect of the $U_p(t)$ ponderomotive shift of the continuum can be identified.

When the duration of the Gaussian laser pulse is reduced from the picosecond regime to a FWHM on the order of a few hundred femtoseconds, owing to the broader bandwidth, a new competing ionization pathway starts to dominate over the $2s \rightarrow 4s \rightarrow$ continuum route (see the Supplemental Material in [66]). According to the multilevel solution, for a FWHM less than 200 fs, the $2s \rightarrow 2p \rightarrow 4d \rightarrow$ continuum pathway already dominates the spectrum (there the emitted electrons are mostly f electrons due to the strong coupling between the $4d$ level and the f continuum). Despite the dominance of the $2s \rightarrow 2p \rightarrow 4d \rightarrow$ continuum route, the above-discussed effects of the bound-state DSSs are still observable in the p channel spectrum after the two-photon Rabi flops between the $2s$ and $4s$ states [66]. This kind of competition of the two ionization pathways is well supported by the TDSE solution, as shown in Fig. 7. Here the peak laser intensity is chosen such that three Rabi cycles are completed between the $2s$ and $4s$ levels. Accordingly, the photoelectron spectrum exhibits pronounced intensity modulations with three distinct peaks. As seen in Fig. 7(a), the $2p$ level and the one-photon resonant $4d$ level also participate in the dynamics when a FWHM of 100 fs is applied. This explains the high peak in the f channel spectrum at $\omega_\varepsilon \approx 1.2$ eV [Fig. 7(b)], which is the result of ionization via the $4d$ state. The emission of p electrons via the $4d$ level is also allowed by the selection rules, but as will be clear below this process has rather low probability and the increased yield at the rightmost peak of the p channel spectrum is attributed to a different reason. The emitted p and f electrons contribute with different weights to the three spectrum peaks, which is reflected by the angular distributions

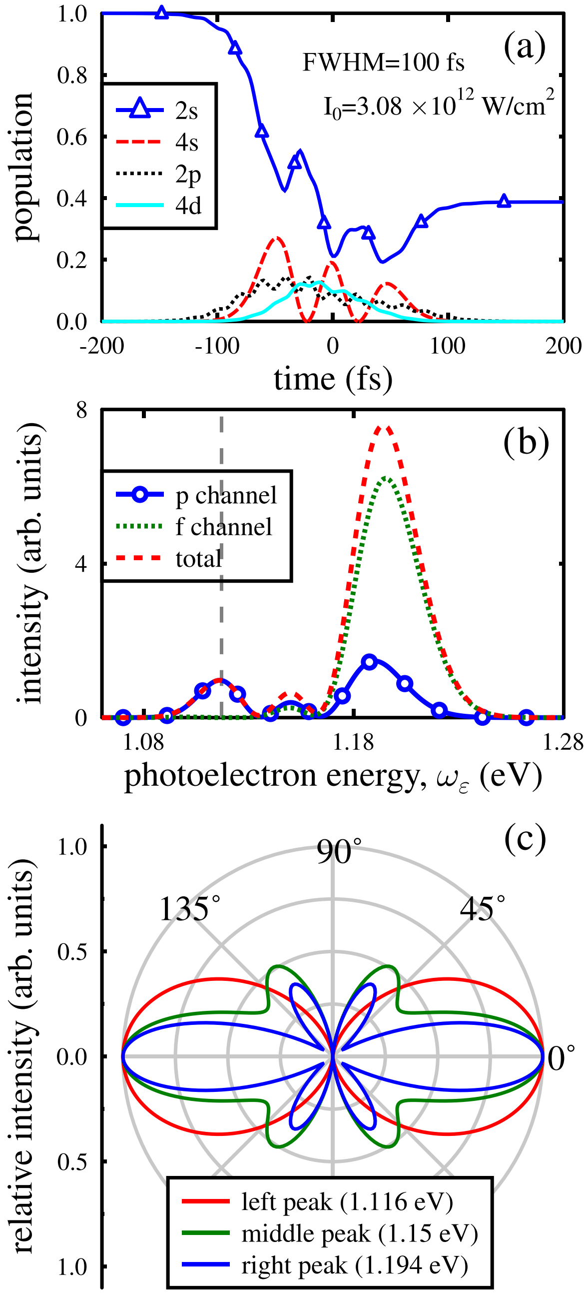

FIG. 7. Resonance-enhanced multiphoton ionization of Li computed by the 3D TDSE method for a two-photon resonant ($\Delta = 0 \rightarrow \omega \approx 2.169$ eV) Gaussian laser pulse of 100-fs FWHM duration and $I_0 = 3.08\times10^{12}$ W/cm^2 peak intensity. (a) Three Rabi cycles are completed by the valence electron between the resonantly coupled $2s$ and $4s$ states, while the intermediate $2p$ state and the one-photon resonant $4d$ state also participate in the dynamics. (b) The corresponding photoelectron spectrum exhibits pronounced intensity modulations with three distinct peaks, which are the result of two competing ionization pathways: (i) the $2s \rightarrow 4s \rightarrow$ continuum pathway and (ii) the $2s \rightarrow 2p \rightarrow 4d \rightarrow$ continuum pathway. (c) The emitted p and f electrons contribute with different weights to the three spectrum peaks, which is also reflected by the angular distributions computed for the three peak energies. Here each curve is normalized to its maximal value.

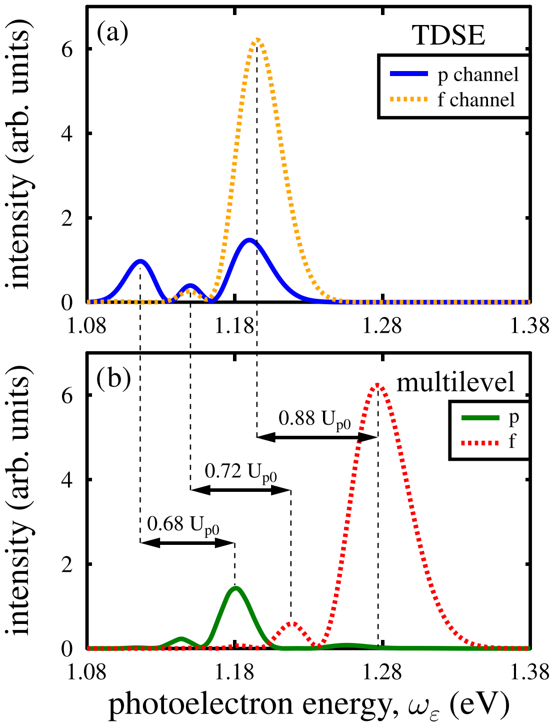

FIG. 8. Comparison between the photoelectron spectra of Li computed with (a) the 3D TDSE method and (b) the multilevel approximation for the laser parameters applied in Fig. 7. In the 3D TDSE method, the ponderomotive motion of the emitted electron is properly described. In contrast, the multilevel solution neglects continuum-continuum couplings and hence cannot account for the dynamic Stark shift of the continuum states. Thus, on the one hand, the time-dependent ponderomotive energy of the continuum states [$U_p(t)$] causes shifting of the spectrum towards lower energies (ranging between approximately 68% and 88% of its peak value U_{p0}). On the other hand, $U_p(t)$ modifies the shape of the spectrum by even changing its symmetry (see the p channel). The rightmost peak of the p channel spectrum remains the highest even when the bound d states are omitted from the 3D TDSE simulations, confirming that it is indeed not the result of ionization via the $2s \rightarrow 2p \rightarrow 4d \rightarrow$ p-continuum pathway.

too in Fig. 7(c). The left peak is built up from p electrons, in the right peak the contribution of f electrons is dominant, and the middle peak is approximately a 60%–40% weighted mixture of p and f electrons, respectively.

A comparison of the photoelectron spectra obtained by the TDSE and the multilevel methods is presented in Fig. 8. Here the overall shapes of these spectra computed by the two different methods are similar, but important qualitative differences are seen in the different channels, which can be attributed to the $U_p(t)$ ponderomotive shift of the continuum. As expected, owing to the increased ionization potential in the strong field, the TDSE spectrum is shifted towards lower photoelectron energies. The observed effective shifts of the individual peaks ranges between approximately 68% and 88% of the peak value of the ponderomotive shift U_{p0}. Importantly, the symmetry of the spectrum is also modified by $U_p(t)$. This is most obvious in the p channel spectrum, but also observable in the f channel. In both channels the electron yield at the higher-energy side of the spectrum gets increased in the TDSE description, compared to the multilevel solution. As a result, the asymmetry of the spectrum in the p channel even changes sign. To fully confirm that the increased p electron yield at the higher-energy peak in the TDSE spectrum is attributed to $U_p(t)$, we carried out a TDSE calculation where the d bound levels are excluded and hence the $2s \rightarrow 2p \rightarrow 4d \rightarrow$ continuum pathway is blocked. The found spectrum of the p electrons still exhibits the same kind of asymmetry as the real spectrum in Fig. 8(a), making clear that the observed change in the asymmetry between the TDSE and multilevel spectra is ascribed to $U_p(t)$.

V. CONCLUSION

Solving the time-dependent Schrödinger equation of the valence electron of Na and Li on increasing levels of complexity, we have demonstrated the important role of bound- and continuum-state dynamic Stark shifts in strong-field excitation and subsequent ionization. Based on the predictions of a minimal model, confirmed by the multilevel solution, we have shown that the relative DSS of the strongly coupled levels can be compensated by optimally detuned pulses, allowing for a high level of control over the system dynamics. This detuning control facilitates the accurate identification of δS_0 in the bound-bound transition frequency shifts observed in resonance-enhanced multiphoton ionization. Studying the three-photon ionization of Li following two-photon Rabi oscillations, the impact of bound- and continuum-state dynamic Stark shifts on the spectral features have been also identified. Based on the nice agreement of the minimal three-level model and the multilevel description, supported by a simple analytical model, we have shown how the DSSs of the involved levels determine the shifting and splitting of the Autler-Townes doublet. Furthermore, we have demonstrated that, besides the magnitude of the DSSs, their temporal profiles also affect the asymmetry of the AT doublet. Comparing the photoelectron spectra obtained by the TDSE method to those calculated from the multilevel description allowed for the identification of the effect of the $U_p(t)$ ponderomotive shift of the continuum. The dynamical shift of the continuum states (i) pushes the spectrum towards lower energies and, importantly, (ii) modifies the spectrum asymmetry.

When considering resonance-enhanced multiphoton ionization in strong fields, the found effects of the bound-state–continuum-state dynamic Stark shifts act simultaneously and the final spectrum shape is determined as their overall impact. The step-by-step exploration of these effects presented here has allowed us to understand and identify the spectral characteristics observed in intense laser fields.

ACKNOWLEDGMENTS

A.C. is grateful for support from the János Bolyai Research Scholarship (Grant No. BO/00474/22/11) of the Hungarian Academy of Sciences. This work was supported by the ÚNKP-22-5 New National Excellence Program of the Ministry for Culture and Innovation from the source of the National Research, Development and Innovation Fund. Support by the COST Action CA18222, AttoChem is acknowledged. Y.Z. acknowledges support from the National Key Research and Development Program of China (Grant No. 2019YFA0308300). The ELI-ALPS project (Project No. GINOP-2.3.6-15-2015-00001) is supported by the European Union and cofinanced by the European Regional Development Fund.

[1] M. Shapiro and P. Brumer, *Principles of the Quantum Control of Molecular Processes* (Wiley, New York, 2003).
[2] K. Bergmann, H. Theuer, and B. W. Shore, Rev. Mod. Phys. **70**, 1003 (1998).
[3] N. B. Delone and V. P. Krainov, Phys.-Usp. **42**, 669 (1999).
[4] B. J. Sussman, Am. J. Phys. **79**, 477 (2011).
[5] B. J. Sussman, D. Townsend, M. Y. Ivanov, and A. Stolow, Science **314**, 278 (2006).
[6] I. R. Solá, B. Y. Chang, and H. Rabitz, J. Chem. Phys. **119**, 10653 (2003).
[7] C. Trallero-Herrero, J. L. Cohen, and T. C. Weinacht, Phys. Rev. Lett. **96**, 063603 (2006).
[8] H. Suchowski, A. Natan, B. D. Bruner, and Y. Silberberg, J. Phys. B **41**, 074008 (2008).
[9] J.-C. Liu, C.-K. Wang, and F. Gel'mukhanov, Phys. Rev. A **76**, 043422 (2007).
[10] C. Trallero-Herrero, D. Cardoza, T. C. Weinacht, and J. L. Cohen, Phys. Rev. A **71**, 013423 (2005).
[11] C. Trallero-Herrero and T. C. Weinacht, Phys. Rev. A **75**, 063401 (2007).
[12] S. Lee, J. Lim, J. Ahn, V. Hakobyan, and S. Guérin, Phys. Rev. A **82**, 023408 (2010).
[13] S. Lee, J. Lim, C. Y. Park, and J. Ahn, Opt. Express **19**, 2266 (2011).
[14] B. Kaufman, T. Rozgonyi, P. Marquetand, and T. C. Weinacht, Phys. Rev. A **102**, 063117 (2020).
[15] R. R. Freeman, P. H. Bucksbaum, H. Milchberg, S. Darack, D. Schumacher, and M. E. Geusic, Phys. Rev. Lett. **59**, 1092 (1987).
[16] J. N. Bardsley, A. Szöke, and M. J. Comella, J. Phys. B **21**, 3899 (1988).
[17] V. C. Reed and K. Burnett, Phys. Rev. A **43**, 6217 (1991).
[18] G. N. Gibson, R. R. Freeman, and T. J. McIlrath, Phys. Rev. Lett. **69**, 1904 (1992).
[19] J. G. Story, D. I. Duncan, and T. F. Gallagher, Phys. Rev. Lett. **70**, 3012 (1993).
[20] R. R. Jones, Phys. Rev. Lett. **74**, 1091 (1995).
[21] S. Hack, S. Majorosi, M. G. Benedict, S. Varró, and A. Czirják, Phys. Rev. A **104**, L031102 (2021).
[22] M. Fushitani, C.-N. Liu, A. Matsuda *et al.*, Nat. Photon. **10**, 102 (2016).
[23] D. Chetty, R. D. Glover, B. A. deHarak, X. M. Tong, H. Xu, T. Pauly, N. Smith, K. R. Hamilton, K. Bartschat, J. P. Ziegel, N. Douguet, A. N. Luiten, P. S. Light, I. V. Litvinyuk, and R. T. Sang, Phys. Rev. A **101**, 053402 (2020).
[24] Y. Zhao, Y. Zhou, J. Liang, Q. Ke, Y. Liao, M. Li, and P. Lu, Phys. Rev. A **106**, 063103 (2022).
[25] M. Krug, T. Bayer, M. Wollenhaupt, C. Sarpe-Tudoran, T. Baumert, S. S. Ivanov, and N. V. Vitanov, New J. Phys. **11**, 105051 (2009).
[26] U. Saalmann, S. K. Giri, and J. M. Rost, Phys. Rev. Lett. **121**, 153203 (2018).
[27] M. Li, P. Zhang, S. Luo, Y. Zhou, Q. Zhang, P. Lan, and P. Lu, Phys. Rev. A **92**, 063404 (2015).
[28] N. A. Hart, J. Strohaber, A. A. Kolomenskii, G. G. Paulus, D. Bauer, and H. A. Schuessler, Phys. Rev. A **93**, 063426 (2016).
[29] A. Bunjac, D. B. Popović, and N. S. Simonović, Phys. Lett. A **394**, 127197 (2021).
[30] B. Kaufman, T. Rozgonyi, P. Marquetand, and T. Weinacht, Phys. Rev. A **103**, 023108 (2021).
[31] S. H. Autler and C. H. Townes, Phys. Rev. **100**, 703 (1955).
[32] D. Rogus and M. Lewenstein, J. Phys. B **19**, 3051 (1986).
[33] X. Tang, A. Lyras, and P. Lambropoulos, J. Opt. Soc. Am. B **7**, 456 (1990).
[34] C. Meier and V. Engel, Phys. Rev. Lett. **73**, 3207 (1994).
[35] A. Adler, A. Rachman, and E. J. Robinson, J. Phys. B **28**, 5077 (1995).
[36] P. V. Demekhin and L. S. Cederbaum, Phys. Rev. A **86**, 063412 (2012).
[37] A. D. Müller, E. Kutscher, A. N. Artemyev, L. S. Cederbaum, and P. V. Demekhin, Chem. Phys. **509**, 145 (2018).
[38] S. B. Zhang and N. Rohringer, Phys. Rev. A **89**, 013407 (2014).
[39] C. Yu and L. B. Madsen, Phys. Rev. A **98**, 033404 (2018).
[40] D. A. Tumakov, D. A. Telnov, G. Plunien, and V. M. Shabaev, Phys. Rev. A **100**, 023407 (2019).
[41] N. S. Simonović, D. B. Popović, and A Bunjac, Atoms **11**, 20 (2023).
[42] A. Tóth and A. Csehi, J. Phys. B **54**, 035005 (2021).
[43] A. Bunjac, D. B. Popović, and N. S. Simonović, Eur. Phys. J. D **76**, 249 (2022).
[44] M. Wollenhaupt, A. Assion, O. Bazhan, C. Horn, D. Liese, C. Sarpe-Tudoran, M. Winter, and T. Baumert, Phys. Rev. A **68**, 015401(R) (2003).
[45] M. Wollenhaupt, A. Präkelt, C. Sarpe-Tudoran, D. Liese, and T. Baumert, J. Opt. B **7**, S270 (2005).
[46] W.-C. Jiang, H. Liang, S. Wang, L.-Y. Peng, and J. Burgdörfer, Phys. Rev. Res. **3**, L032052 (2021).
[47] S. Nandi, E. Olofsson, M. Bertolino, S. Carlström, F. Zapata, D. Busto, C. Callegari, M. Di Fraia, P. Eng-Johnsson, R. Feifel, G. Gallician, M. Gisselbrecht, S. Maclot, L. Neoričić, J. Peschel, O. Plekan, K. C. Prince, R. J. Squibb, S. Zhong, P. V. Demekhin *et al.*, Nature (London) **608**, 488 (2022).
[48] X. Zhang, Y. Zhou, Y. Liao, Y. Chen, J. Liang, Q. Ke, M. Li, A. Csehi, and P. Lu, Phys. Rev. A **106**, 063114 (2022).
[49] A. Assion, T. Baumert, J. Helbing, V. Seyfried, and G. Gerber, Chem. Phys. Lett. **259**, 488 (1996).
[50] A. Bunjac, D. B. Popović, and N. S. Simonović, Eur. Phys. J. D **71**, 208 (2017).
[51] A. Bunjac, D. B. Popović, and N. S. Simonović, Phys. Chem. Chem. Phys. **19**, 19829 (2017).
[52] Y. Boran, N. Hart, N. Kaya, J. Zhou, A. A. Kolomenskii, and H. A. Schuessler, J. Phys. B **54**, 145401 (2021).
[53] A. Tóth and A. Csehi, Phys. Rev. A **104**, 063102 (2021).
[54] T. Morishita and C. D. Lin, Phys. Rev. A **87**, 063405 (2013).
[55] S.-D. Jheng and T. F. Jiang, J. Phys. B **50**, 195001 (2017).

[56] M. Schuricke, K. Bartschat, A. N. Grum-Grzhimailo, G. Zhu, J. Steinmann, R. Moshammer, J. Ullrich, and A. Dorn, Phys. Rev. A **88**, 023427 (2013).

[57] M. Schuricke, G. Zhu, J. Steinmann, K. Simeonidis, I. Ivanov, A. Kheifets, A. N. Grum-Grzhimailo, K. Bartschat, A. Dorn, and J. Ullrich, Phys. Rev. A **83**, 023413 (2011).

[58] P. V. Demekhin and L. S. Cederbaum, Phys. Rev. A **83**, 023422 (2011).

[59] L. Dalcin, P. Kler, R. Paz, and A. Cosimo, Adv. Water Resour. **34**, 1124 (2011).

[60] H. Hellmann, J. Chem. Phys. **3**, 61 (1935).

[61] M. S. Pindzola *et al.*, J. Phys. B **40**, R39 (2007).

[62] T. N. Rescigno and C. W. McCurdy, Phys. Rev. A **62**, 032706 (2000).

[63] T. J. Park and C. J. Light, J. Chem. Phys. **85**, 5870 (1986).

[64] W.-C. Jiang and X.-Q. Tian, Opt. Express **25**, 26832 (2017).

[65] A. Messiah, *Quantum Mechanics* (North-Holland, Amsterdam, 1961), Vol. II.

[66] See Supplemental Material at http://link.aps.org/supplemental/10.1103/PhysRevA.107.053101 for (i) the calculated Stark shifts and Rabi frequencies of Na and Li, (ii) the pulse duration dependence of population dynamics of Na and Li in two-photon transitions, (iii) the pulse duration dependence of the photoelectron spectrum of Li following three-photon ionization, and (iv) the time dependence of the photoelectron spectrum obtained by the TDSE method.

[67] M. Baghery, U. Saalmann, and J. M. Rost, Phys. Rev. Lett. **118**, 143202 (2017).